Research Square

Preprints are preliminary reports that have not undergone peer review.
They should not be considered conclusive, used to inform clinical practice,
or referenced by the media as validated information.

Pauli dynamics and finite-gap Stern-Gerlach corrections from a spinorial SU(2) rotor

Shengliang Dong

else3.com@outlook.com

Chengdu Element Universe Technology Co., Ltd. https://orcid.org/0009-0007-0074-6119

Research Article

Keywords: Stern-Gerlach effect, Pauli equation, SU(2) rotor, effective field theory, quantum foundations, wavepacket dynamics

Posted Date: September 9th, 2026

DOI: https://doi.org/10.21203/rs.3.rs-10971056/v1

License: This work is licensed under a Creative Commons Attribution 4.0 International License.
Read Full License

Additional Declarations: The authors declare no competing interests.

Pauli dynamics and finite-gap Stern–Gerlach corrections from a spinorial SU(2) rotor

Shengliang Dong

Chengdu Element Universe Technology Co., Ltd.

No.18, Floor 12, Unit 1, Building 3, No.700 Datian Road, Dafeng Street, Xindu District, Chengdu, Sichuan 610

else3.com@outlook.com

ORCID: 0009-0007-0074-6119

Abstract

The Pauli equation describes Stern–Gerlach splitting through a two-dimensional spin sector, but it leaves open how that sector could arise as the low-energy multiplet of a finite-gap internal system. We construct a centre-odd SU(2) rotor with fixed body weight $q = 1/2$ and a magnetic moment fixed to its body axis. The standard direction-cosine projection gives $Pn_iP = \sigma_i/3$, fixing the Pauli normalization. Eliminating the $j = 3/2$ multiplet at gap $\Delta = 3\hbar^2/(2I)$ produces a common $-2\mu^2|\boldsymbol{B}|^2/\Delta$ potential and a cubic spin correction $8\mu^3|\boldsymbol{B}|^2\boldsymbol{\sigma}\cdot\boldsymbol{B}/(5\Delta^2)$. A pure $\boldsymbol{J}\cdot\boldsymbol{B}$ coupling is included as a block-diagonal control. In a Maxwell-consistent two-dimensional Stern–Gerlach field, dressed-state propagation gives a total-centroid correction of -0.277119 packet widths; switching only the cubic term changes the centroid by 7.7620×10^{-4} widths. The full-rotor density differs from the cubic effective theory by 1.54×10^{-4} in integrated L^1 norm, whereas the generator control coincides with Pauli dynamics. Gap scans recover the predicted inverse-gap and inverse-gap-squared exponents. The result is a reproducible effective rotor model for a framed SU(2) internal degree of freedom, with laboratory bounds set by common-mode beam measurements.

Keywords: Stern–Gerlach experiment; quantum rotor; SU(2) holonomy; effective Hamiltonian; wave-packet dynamics

1 Introduction

The Stern–Gerlach experiment established spatial quantization in an inhomogeneous magnetic field [1]. Its nonrelativistic dynamics is accurately described by a Pauli spinor propagating under $-\mu\boldsymbol{\sigma}\cdot\boldsymbol{B}$. Wave-packet calculations resolve the two branches, their finite overlap, and the role of the magnet geometry [2, 3]. Atom-chip experiments now extend this control to coherent momentum splitting, reversal and recombination [4, 5, 6]. These advances make a precise low-energy question meaningful: if the Pauli doublet is the lowest multiplet of a larger internal system, which beam observables retain the first finite-gap correction?

Quantum-rotor descriptions of spin provide a natural setting for this question. Bohm, Schiller and Tiomno represented the Pauli equation using orientation variables [7, 8]; related geometric constructions were developed by Holland and others [9, 10, 11]. Symmetric-top spectroscopy supplies the complementary fact that a moment fixed to a body axis couples through a direction cosine and inherits the standard $q/[j(j+1)]$ projection factor [12, 13]. The sign change under a 2π rotation and recovery after 4π are also experimentally established spinor properties [14, 15]. The problem addressed here begins after these facts: retain the higher rotor tower, derive its low-energy remainder, and identify a spatial observable that distinguishes it from an exactly block-diagonal spin coupling.

Loop quantum gravity (LQG) provides a kinematical motivation for retaining that tower. Its graph states carry SU(2) holonomies, fluxes and half-integer spin-network labels [16, 17], while canonical matter constructions attach fermionic data to graph vertices [18, 19, 20, 21]. The link studied here is between a specified node-local SU(2) degree of freedom and laboratory Pauli dynamics, including an explicit approximation parameter and an observable remainder.

We formulate an effective model on a fixed semiclassical spin-network background. A framed node retains an untraced holonomy $U \in \mathrm{SU}(2)$. Centre oddness selects half-integer representations, and a fixed right weight $q = 1/2$ removes the body-frame degeneracy of the free SU(2) rotor. A laboratory field is resolved on the local triad. The main interaction is the direction-cosine coupling of a body-fixed moment. The equally covariant generator coupling is

retained as a control, allowing the finite-gap response to be attributed to a physical operator choice rather than to the existence of a gap alone.

Three results follow. The lowest internal sector is a two-dimensional $j = 1/2$ multiplet with the usual 4π return, and the direction-cosine theorem fixes its Pauli normalization. Schrieffer–Wolff elimination [22, 23] gives a common quadratic potential and a cubic change in the spin splitting. Full two-dimensional propagation, initialized in the dressed low-energy subspace, then resolves both terms without a discontinuous spatial branch cut. The common centroid scales as Δ^{-1}, the cubic switch as Δ^{-2}, and a pure $\boldsymbol{J} \cdot \boldsymbol{B}$ control remains exactly Pauli-like.

2 Spinorial SU(2) rotor sector

2.1 Framed node and state space

Consider one node of a spin network after choosing a local semiclassical triad $e_i{}^a$. A traced Wilson loop retains a class function. Here the matrix-valued holonomy is kept at a framed node, as illustrated in Fig. 1; its open node index is contracted with the remaining incident-link and matter data when gauge-invariant amplitudes are formed. Spinor and framed descriptions of LQG variables provide closely related kinematical settings [24].

The one-particle state space is

$$\mathcal{H} = L^2(\mathbb{R}^3, d^3x) \otimes \mathcal{H}^{(-)}_{q=1/2}, \tag{1}$$

where the internal functions satisfy

$$\psi(-U) = -\psi(U), \tag{2}$$

$$\psi\Big(U e^{-i\alpha\sigma_3/2}\Big) = e^{-iq\alpha}\psi(U), \qquad q = \frac{1}{2}. \tag{3}$$

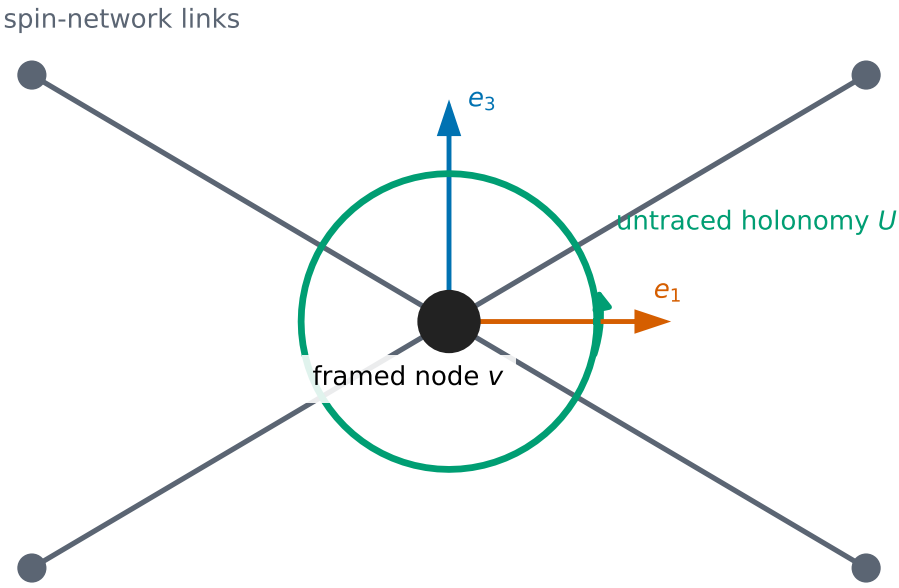


Figure 1: Projected view of a framed spin-network node. The green based loop denotes an untraced SU(2) holonomy U; e_1 and e_3 are axes of the local triad used to resolve the laboratory magnetic field.

The right-equivariance condition fixes the body weight on the quotient of SU(2) by its U(1) subgroup, as in the Wigner-function and monopole-harmonic descriptions [25, 26].

Peter–Weyl decomposition gives

$$\Psi(\boldsymbol{x}, U) = \sum_{j=1/2,\,3/2,\ldots} \sum_{m=-j}^{j} \psi_{jm}(\boldsymbol{x}) \sqrt{2j+1}\, D^{j}_{m,1/2}(U). \tag{4}$$

Since $D^j(-U) = (-1)^{2j} D^j(U)$, centre oddness selects the half-integer tower. Fixed q leaves $2j+1$ states at each level, so the lowest $j = 1/2$ multiplet is exactly two-dimensional.

2.2 Free spectrum and spinorial return

The left SU(2) action rotates the m index. Its central element represents a 2π rotation and multiplies the retained states by -1; the second application restores the state. The free

internal Hamiltonian is

$$H_{\rm rot} = \frac{\hbar^2}{2I}\boldsymbol{J}^2, \qquad I > 0, \tag{5}$$

with $E_j = \hbar^2 j(j+1)/(2I)$. Thus

$$\Delta = E_{3/2} - E_{1/2} = \frac{3\hbar^2}{2I}. \tag{6}$$

This is the SU(2) double-cover analogue of a fixed-body-weight symmetric top: the direction-cosine algebra is shared with molecular rotation, while the half-integer j, q tower supplies the spinorial return.

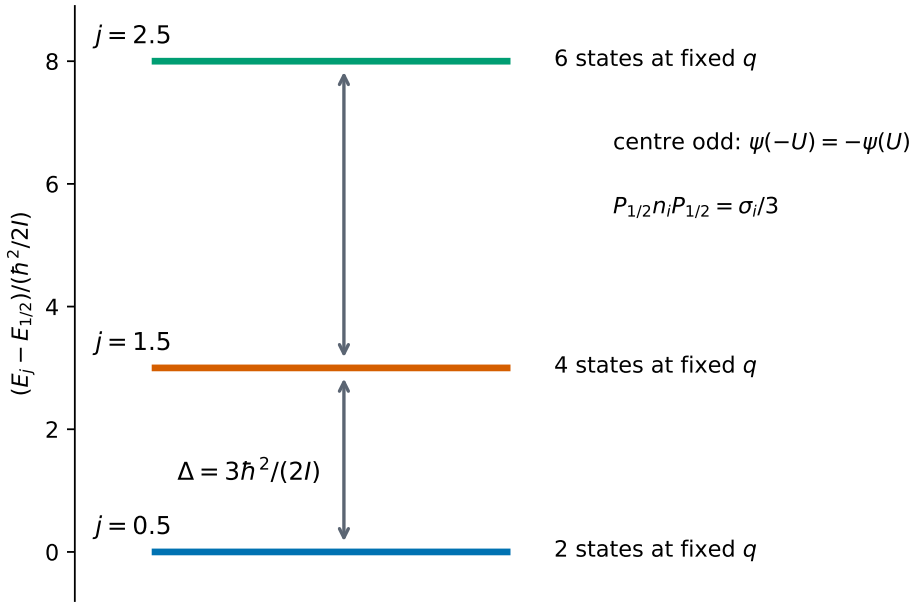


Figure 2: Centre-odd rotor spectrum at fixed $q = 1/2$. The ground doublet is separated from the $j = 3/2$ multiplet by Δ. The body-axis direction operator connects adjacent multiplets, whereas $\boldsymbol{J}$ acts within each fixed-j block.

2.3 Two covariant magnetic couplings

Let $B_a(\boldsymbol{x})$ be a laboratory magnetic field and $B_i = e_i{}^a B_a$ its components in the node frame. Both the left generator J_i and the body-axis direction $n_i(U) = D^1_{i0}(U)$ transform as internal

vectors. The rank-one interaction can therefore be written

$$H_B = -a\,\boldsymbol{J}\cdot\boldsymbol{B} - b\,\boldsymbol{n}\cdot\boldsymbol{B}. \tag{7}$$

The body-axis model studied below takes $a = 0$: its magnetic moment follows the rotor orientation, as in symmetric-top spectroscopy. The endpoint $b = 0$ is a useful control because $\boldsymbol{J}$ is block diagonal in j. Section 3 fixes both endpoints to the same measured Pauli moment μ, so their finite-gap responses can be compared without changing the low-energy Hamiltonian.

3 Pauli projection and finite-gap Hamiltonian

The direction operator $n_p = D^1_{p0}(U)$ is centre even and obeys the usual rank-one selection rules. Its projection and the finite-gap expansion are derived below with exact Wigner $3j$ symbols; the coupling normalization is fixed before any wave-packet calculation.

3.1 Exact ground-block normalization

With normalized Wigner functions $|jmq\rangle$, the direction operator has matrix elements

$$\langle j'm'q|n_p|jmq\rangle = (-1)^{m'-q}\sqrt{(2j'+1)(2j+1)}\begin{pmatrix} j' & 1 & j \\ -m' & p & m\end{pmatrix}\begin{pmatrix} j' & 1 & j \\ -q & 0 & q\end{pmatrix}. \tag{8}$$

The standard projection theorem for a body-axis vector gives

$$P_j n_i P_j = \frac{q}{j(j+1)} P_j J_i P_j. \tag{9}$$

For $j = q = 1/2$, $PJ_iP = \sigma_i/2$, hence

$$Pn_iP = \frac{1}{3}\sigma_i. \tag{10}$$

Projecting Eq. (7) therefore yields the Pauli interaction provided

$$\frac{a}{2}+\frac{b}{3}=\mu. \tag{11}$$

This line contains two informative endpoints. The body-axis model has $(a,b)=(0,3\mu)$; the generator control has $(a,b)=(2\mu,0)$. Their ground blocks are identical, but only the body-axis operator has matrix elements between different j multiplets.

The full body-axis Hamiltonian is

$$H=\frac{\boldsymbol{p}^2}{2M}+\frac{\hbar^2}{2I}\boldsymbol{J}^2-3\mu\,\boldsymbol{n}\cdot\boldsymbol{B}(\boldsymbol{x}). \tag{12}$$

3.2 Finite-gap expansion

For an axial field, m is conserved. Writing $s=+1$ for $m=+1/2$ and $s=-1$ for $m=-1/2$, the relevant $j=1/2,3/2$ block, after subtracting $E_{1/2}$, is

$$H_s=\begin{pmatrix} -s\mu B & -\sqrt{2}\mu B \\ -\sqrt{2}\mu B & \Delta-s\mu B/5 \end{pmatrix}. \tag{13}$$

The entries follow directly from Eq. (8):

$$\left\langle \tfrac{1}{2},\tfrac{1}{2}\middle|n_0\middle|\tfrac{1}{2},\tfrac{1}{2}\right\rangle=\frac{1}{3},\quad \left\langle \tfrac{3}{2},\tfrac{1}{2}\middle|n_0\middle|\tfrac{1}{2},\tfrac{1}{2}\right\rangle=\frac{\sqrt{2}}{3},\quad \left\langle \tfrac{3}{2},\tfrac{1}{2}\middle|n_0\middle|\tfrac{3}{2},\tfrac{1}{2}\right\rangle=\frac{1}{15}. \tag{14}$$

The lower exact eigenvalue is

$$\varepsilon_s(B)=\frac{1}{2}\left[\Delta-\frac{6s}{5}\mu B-\sqrt{\left(\Delta+\frac{4s}{5}\mu B\right)^2+8\mu^2B^2}\right]. \tag{15}$$

Its low-field expansion is

$$\varepsilon_s(B)=-s\mu B-\frac{2\mu^2B^2}{\Delta}+s\frac{8\mu^3B^3}{5\Delta^2}+O\!\left(\frac{\mu^4B^4}{\Delta^3}\right). \tag{16}$$

Because a rank-one operator changes j by at most one, no path through $j \geq 5/2$ returns to the ground block in three insertions. The displayed coefficients are therefore independent of the internal cutoff.

Rotational covariance gives the local effective Hamiltonian

$$H_{\mathrm{eff}}^{\mathrm{loc}} = \frac{\boldsymbol{p}^2}{2M} + E_{1/2} - \frac{2\mu^2|\boldsymbol{B}|^2}{\Delta}\mathbf{1} + \left[-\mu + \frac{8\mu^3|\boldsymbol{B}|^2}{5\Delta^2}\right]\boldsymbol{\sigma}\cdot\boldsymbol{B} + O\left(\frac{\mu^4|\boldsymbol{B}|^4}{\Delta^3}\right). \tag{17}$$

For a spatially varying field, the local block transformation $W(\boldsymbol{x})$ also converts the kinetic operator into

$$\frac{(\boldsymbol{p}-\boldsymbol{\mathcal{A}})^2}{2M} + \Phi, \qquad \mathcal{A}_i = i\hbar W^\dagger \partial_i W, \qquad \Phi = \frac{\hbar^2}{2M}(\partial_i W)^\dagger(1 - WW^\dagger)(\partial_i W). \tag{18}$$

The full-rotor propagation contains these derivative effects automatically; comparison with Eq. (17) measures their combined remainder. In addition to $r = \mu B_{\max}/\Delta$, we monitor

$$\eta_{\mathrm{kin}} = \frac{\hbar^2}{2M\sigma^2\Delta}, \qquad \eta_G = \frac{\mu G\sigma}{\Delta}. \tag{19}$$

Equation (11) separates two physical mechanisms that share the same Pauli limit. The generator endpoint is exactly block diagonal, so a finite rotor gap alone produces no correction. The body-axis endpoint links $j = 1/2$ to $j = 3/2$, and its transition amplitude fixes both the quadratic and cubic terms in Eq. (17). This controlled comparison is used throughout the numerical analysis.

4 Finite-gap beam observables

Equation (17) separates the leading departure from Pauli dynamics into

$$V_{\mathrm{c}}(\boldsymbol{x}) = -\frac{2\mu^2|\boldsymbol{B}|^2}{\Delta}, \tag{20}$$

$$V_{\mathrm{s}}(\boldsymbol{x}) = \frac{8\mu^3|\boldsymbol{B}|^2}{5\Delta^2}\boldsymbol{\sigma}\cdot\boldsymbol{B}. \tag{21}$$

Their force operators are

$$\boldsymbol{F}_{\mathrm{c}} = \frac{2\mu^2}{\Delta}\boldsymbol{\nabla}|\boldsymbol{B}|^2, \qquad \boldsymbol{F}_{\mathrm{s}} = -\frac{8\mu^3}{5\Delta^2}\boldsymbol{\nabla}\left(|\boldsymbol{B}|^2\boldsymbol{\sigma}\cdot\boldsymbol{B}\right). \tag{22}$$

The first translates the complete density at order Δ^{-1}; the second modifies the spin-resolved response at order Δ^{-2}.

For a bias-dominated region with $B_z \simeq B_0 - Gz$, the common acceleration and leading displacement are

$$a_{\mathrm{c}} \simeq -\frac{4\mu^2 B_0 G}{M\Delta}, \qquad \delta z_{\mathrm{c}} \simeq -\frac{2\mu^2 B_0 G\tau^2}{M\Delta}. \tag{23}$$

A common-centroid resolution ε_z therefore probes

$$\Delta > \frac{2\mu^2|B_0 G|\tau^2}{M\varepsilon_z}. \tag{24}$$

The primary numerical observable is the smooth total-density centroid

$$\langle z\rangle = \frac{\int z\rho(\boldsymbol{x})\,d^2x}{\int \rho(\boldsymbol{x})\,d^2x}, \qquad \delta\langle z\rangle = \langle z\rangle_{\mathrm{rotor}} - \langle z\rangle_{\mathrm{Pauli}}. \tag{25}$$

It isolates the common mode without assigning density near $z = 0$ to either spatial branch. If $W(\boldsymbol{x})$ is the local two-state isometry, the dressed readout $\phi = W^\dagger\Psi$ also gives component

weights and centroids

$$w_s = \int |\phi_s|^2 d^2x, \qquad z_s = \frac{\int z|\phi_s|^2 d^2x}{w_s}, \qquad s = \uparrow, \downarrow . \tag{26}$$

The cubic response is isolated by a matched effective propagation with $V_{\rm s}$ switched on and off. Finally,

$$P_{\rm leak} = \int \left| (1 - WW^\dagger)\Psi \right|^2 d^2x \tag{27}$$

measures nonadiabatic departure from the dressed low-energy manifold. The bare $j \geq 3/2$ weight is reported separately because it includes the static dressing required by the body-axis interaction.

5 Dressed Stern–Gerlach wave-packet dynamics

5.1 Field, packet and dressed preparation

A one-component field of the form $B_z = B_0 - Gz$ is useful for illustrating the Stern–Gerlach force but violates $\boldsymbol{\nabla} \cdot \mathbf{B} = 0$ if used as a complete local magnetic field. We instead use the current-free linear transverse field

$$\mathbf{B}(x, z) = (Gx, 0, B_0 - Gz). \tag{28}$$

It follows directly that

$$\boldsymbol{\nabla} \cdot \mathbf{B} = G - G = 0, \qquad \boldsymbol{\nabla} \times \mathbf{B} = \mathbf{0}. \tag{29}$$

The bias B_0 prevents a field zero in the packet domain and makes the local quantization direction predominantly axial. The transverse component is retained in all two-dimensional simulations rather than discarded after the Maxwell check.

Equation (28) describes the active transverse region of an idealized magnet. The finite interaction time parameterizes the longitudinal transit through this region; a measured

three-dimensional field map can replace the analytic profile in the same propagation scheme.

For an initial packet width σ, translational mass M, and magnetic moment μ, we use the recoil scales

$$t_0 = \frac{M\sigma^2}{\hbar}, \qquad E_0 = \frac{\hbar}{t_0}, \qquad \mathbf{r} = \sigma\tilde{\mathbf{r}}, \qquad t = t_0\tilde{t}. \tag{30}$$

If B_{s} denotes the chosen field scale, then $\mathbf{B} = B_{\mathrm{s}}\tilde{\mathbf{B}}$. The dimensionless gradient and rotor gap are

$$g = \frac{\mu G \sigma t_0}{\hbar}, \qquad \delta = \frac{\Delta t_0}{\hbar}. \tag{31}$$

All reported propagation parameters are expressed using these definitions; physical-unit examples, when quoted, are obtained by the inverse maps in Eq. (30) rather than by a separate numerical model.

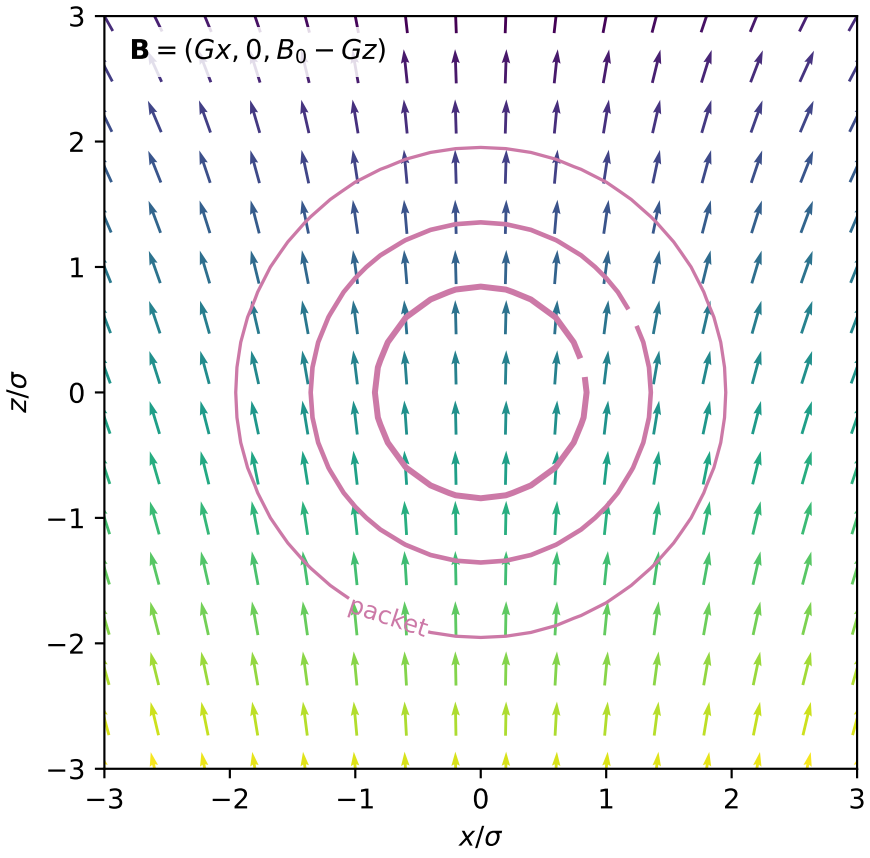


Figure 3: Current-free transverse field used in the propagation. Arrows show $\boldsymbol{B} = (Gx, 0, B_0 - Gz)$, colour gives its magnitude, and magenta contours show the initial Gaussian density.

In dimensionless variables the bare two-component packet is

$$\psi(\boldsymbol{r},0)=\mathcal{N}\exp\!\left[-\frac{x^2+z^2}{4\sigma^2}\right]\chi, \qquad \chi=\frac{1}{\sqrt{2}}\begin{pmatrix}1\\1\end{pmatrix}. \tag{32}$$

To prepare the corresponding full-rotor state in a nonzero field, let $P_{\mathrm{low}}(\boldsymbol{x})$ project onto the two lowest local internal eigenstates and let E embed the bare $j=1/2$ basis. We use the canonical isometry

$$W=P_{\mathrm{low}}E\left(E^{\dagger}P_{\mathrm{low}}E\right)^{-1/2}, \qquad W^{\dagger}W=\mathbf{1}_2, \tag{33}$$

and initialize $\Psi(\boldsymbol{x},0)=W(\boldsymbol{x})\psi(\boldsymbol{x},0)$. Since Eq. (33) depends on the spectral projector, it is invariant under phase choices and unitary rotations of the numerical low-energy eigenvectors. This preparation removes the sudden-field quench while preserving the initial spatial density.

5.2 Matched dynamical models

Five evolutions use the same field, packet and translational propagator:

1. the Pauli Hamiltonian
$$H_{\mathrm{P}}=\frac{\boldsymbol{p}^2}{2M}-\mu\boldsymbol{\sigma}\cdot\boldsymbol{B}; \tag{34}$$
2. Eq. (17) without the cubic term;
3. the same effective Hamiltonian including the cubic term;
4. the full body-axis rotor, Eq. (12);
5. the generator control $(a,b)=(2\mu,0)$.

The last model has the Pauli ground block but no inter-multiplet coupling. It therefore separates finite-gap effects of the body-axis operator from effects that would follow from the rotor spectrum alone.

Time evolution uses the symmetric split operator

$$\Psi(t+\delta t) = e^{-iT\delta t/(2\hbar)} e^{-iV\delta t/\hbar} e^{-iT\delta t/(2\hbar)} \Psi(t) + O(\delta t^3), \tag{35}$$

with Fourier kinetic steps and exact diagonalization of the local Hermitian internal matrix [27].

Table 1: Dimensionless publication baseline. Here $\hbar = M = \mu = \sigma = 1$.

Quantity	Value
Spatial domain and grid	$[-12, 12]^2$, 144×144
Bias and gradient	$B_0 = 20,\ G = 2$
Maximum field	$B_{\max} = 50.12$
Rotor gap and cutoff	$\Delta = 650,\ j_{\max} = 5/2$
Time step and duration	$\delta t = 0.003125,\ \tau = 1.5$
Field ratio	$\mu B_0/\Delta = 0.03077$, $r_{\max} = 0.07711$
Kinetic ratio	$\eta_{\text{kin}} = 7.69 \times 10^{-4}$
Gradient ratio	$\eta_G = 3.08 \times 10^{-3}$

5.3 Verification and refinement

Symbolic tests verify Hermiticity, the vector commutator $[J_i, n_j] = i\epsilon_{ijk} n_k$, the projection theorem and all matrix elements in Eq. (14). Propagation tests recover the Ehrenfest acceleration and the Pauli analyzer weights at five input angles. The generator control is required to reproduce the Pauli density and to retain zero higher-j population.

The spatial grids are 96^2, 144^2 and 216^2, with a common refinement ratio. Time steps 0.0125, 0.00625 and 0.003125 are compared at fixed duration. Domain half-widths 8, 10 and 12 use grids 128^2, 160^2 and 192^2, respectively, so that the spacing is fixed. Internal cutoffs are $j_{\max} = 3/2, 5/2, 7/2$. For resolved observables, the finest pair must differ by less than 1%; an absolute change below 10^{-8} accepts quantities already beneath the numerical reporting floor. Three-level Richardson estimates are used when successive differences have a stable sign. Norm conservation tests the implementation, while convergence is determined from the physical observables. Complete records appear in Appendix B.

6 Results and Discussion

6.1 Coupling control and finite-gap density

The algebra already determines the low-energy limit: both endpoints of Eq. (11) have the same Pauli ground block. The numerical generator control confirms the stronger statement. Its final density is identical to the Pauli density to machine precision, and its higher-j population remains zero. A finite spectrum therefore produces a beam correction only when the probe operator links its multiplets.

For the body-axis rotor, the final total centroids are

$$\langle z\rangle_{\mathrm{P}} = -0.00073217, \tag{36}$$

$$\langle z\rangle_{\mathrm{eff}}^{(2)} = -0.27892919, \tag{37}$$

$$\langle z\rangle_{\mathrm{eff}}^{(3)} = -0.27815299, \tag{38}$$

$$\langle z\rangle_{\mathrm{rotor}} = -0.27785113. \tag{39}$$

Thus

$$\delta\langle z\rangle_{\mathrm{rotor}} = -0.2771190, \qquad \delta\langle z\rangle_{\mathrm{cubic}} = 7.7620 \times 10^{-4}. \tag{40}$$

The first value is the full correction relative to Pauli propagation. The second is obtained by switching only V_{s} in the effective model and therefore isolates the cubic response.

The dressed spin-up and spin-down centroid corrections are -0.2775040 and -0.2771191, respectively; the spin-up weight changes by -4.35×10^{-5}. These internal projections supplement the total centroid without assigning overlapping density to spatial half-planes.

In Fig. 4(a), the integrated L^1 density difference is 0.14155 between the full rotor and Pauli models, but only 1.54×10^{-4} between the full rotor and the cubic effective Hamiltonian, as seen in Fig. 4(c). The effective coefficients were fixed by Eq. (16); no propagation output enters their normalization.

The final bare higher-j weight is 2.0830×10^{-3}. In contrast, the probability outside the

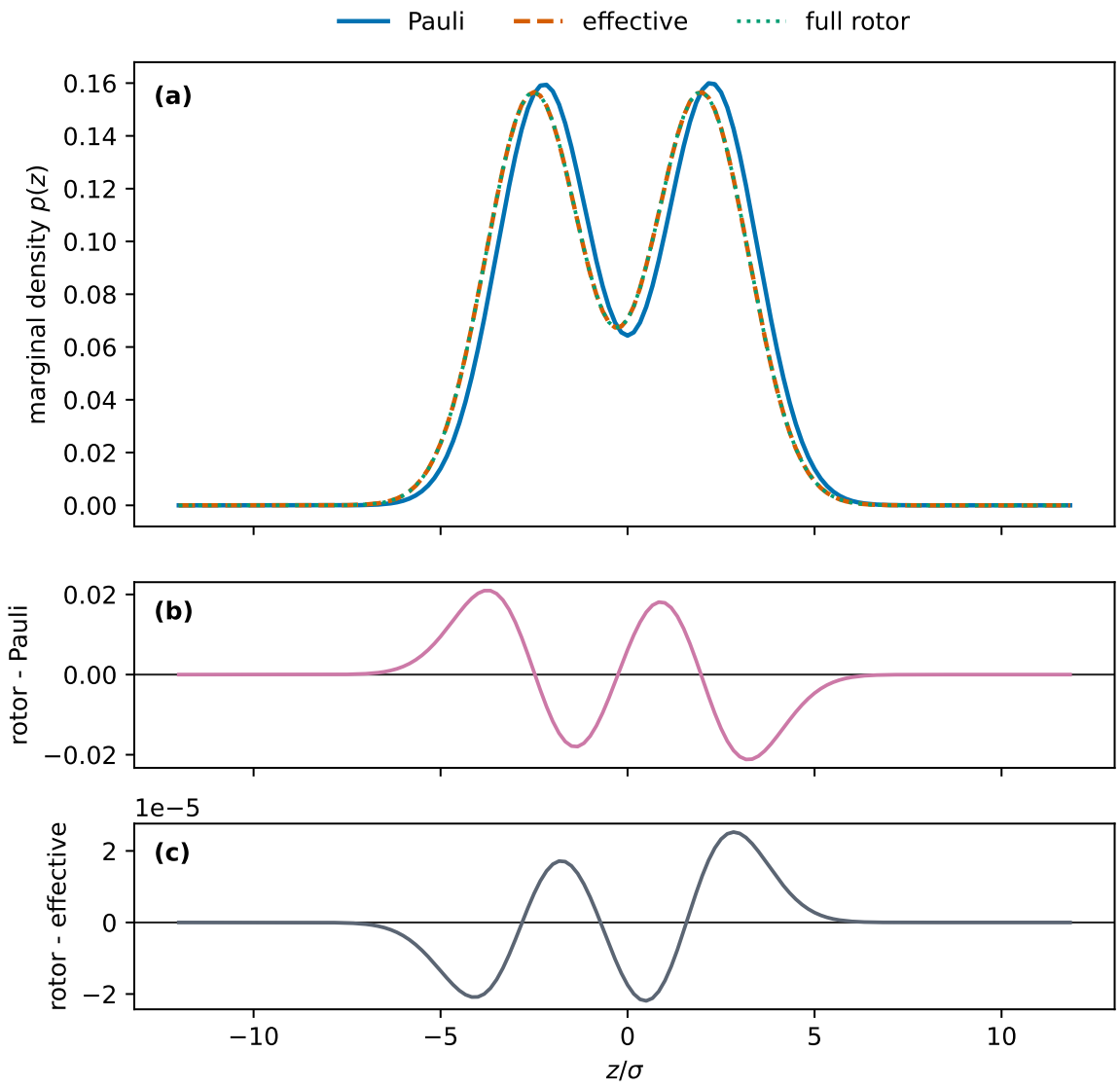


Figure 4: Final marginal densities at the baseline of Table 1. Panel (a) compares the Pauli, effective, and full-rotor marginal densities; panel (b) shows the full-rotor residual relative to Pauli propagation; and panel (c) magnifies the residual relative to the cubic effective Hamiltonian.

local dressed low-energy manifold is

$$P_{\mathrm{leak}} = 1.63 \times 10^{-10}. \tag{41}$$

The separation of these two numbers shows that the bare population is mainly static dressing. Across the refinement study the leakage remains below 6×10^{-9}, so it is reported as an upper-scale diagnostic rather than as a resolved transition signal.

6.2 Convergence and inverse-gap scaling

Figure 5(a) reports observable-specific finest-pair changes. Among changes above the 10^{-8} absolute reporting floor, the largest relative value is 3.25×10^{-5}; the largest absolute change is 1.27×10^{-7}. The cubic-switch sequence has time-step order 2.004 and Richardson limit 7.76206×10^{-4}. The largest norm error in the refinement records is 2.52×10^{-13}, and the largest final-domain boundary-to-peak ratio is 3.00×10^{-12}.

For $r = 0.01, 0.02, 0.04, 0.06$, log–log fits give

$$|\delta\langle z\rangle| \propto r^{0.9998}, \qquad |\delta\langle z\rangle_{\mathrm{cubic}}| \propto r^{2.0037}, \qquad P^{\mathrm{bare}}_{j\geq 3/2} \propto r^{1.9994}. \tag{42}$$

The total centroid follows the quadratic energy term, which is linear in $1/\Delta$; the switched cubic term and static dressing weight follow the predicted quadratic dependence on $1/\Delta$. The points at $r = 0.08$ and 0.10 are displayed as the edge of the declared perturbative interval and are excluded from these leading-slope fits.

6.3 What selects the finite-gap response

The comparison between the two endpoints of Eq. (11) identifies the operative assumption. A finite SU(2) tower and a Pauli ground block do not by themselves imply a correction: the generator coupling is exactly block diagonal. The body-axis coupling supplies the

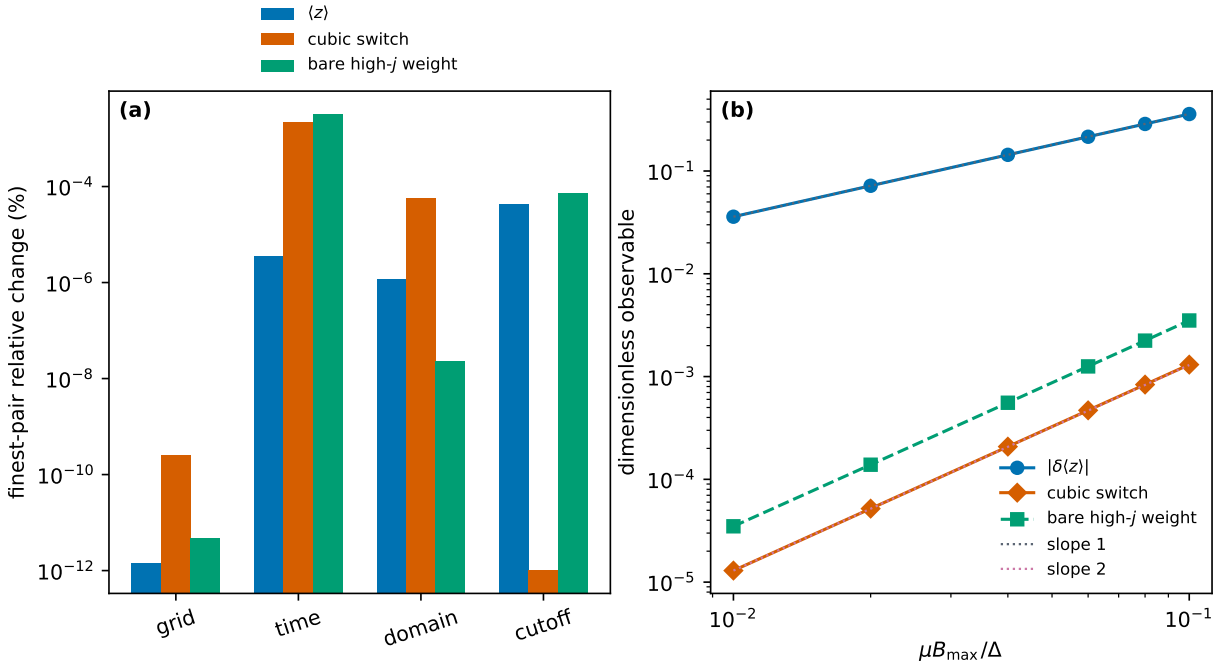


Figure 5: Numerical controls and gap scaling. Panel (a) shows finest-pair changes for the total-centroid correction, cubic switch, and bare higher-j weight on each refinement axis. Panel (b) shows the same observables versus $r = \mu B_{\max}/\Delta$, with unit and quadratic reference slopes.

missing inter-multiplet matrix elements. Its physical meaning is familiar from symmetric-top spectroscopy, while its half-integer fixed-weight sector belongs to the SU(2) double cover. The observable remainder is therefore tied to a defined magnetic-moment geometry rather than to an arbitrary enhancement function.

The LQG role is kinematical. Untraced holonomies, half-integer labels and local SU(2) frames are standard spin-network data. The construction assigns a finite-gap dynamics and a body-axis probe to one such framed local degree of freedom. The prescribed triad maps the laboratory field B_a to internal components B_i; electromagnetic U(1) and gravitational SU(2) retain their separate gauge meanings. This identifies a concrete condition that a future semiclassical LQG derivation can test: whether its node dynamics selects the centre-odd fixed-weight sector and a direction-cosine probe.

6.4 Laboratory scale of the gap bound

Equation (24) can be read directly in SI units. Using the 2022 CODATA constants [28], a Bohr magneton, the mass of a silver atom, $B_0 = 1\,\mathrm{T}$, $G = 10^3\,\mathrm{T\,m^{-1}}$, $\tau = 1\,\mathrm{ms}$ and $\varepsilon_z = 1\,\mu\mathrm{m}$ gives

$$\Delta > 5.99\,\mathrm{eV}, \qquad I < 1.74 \times 10^{-50}\,\mathrm{kg\,m^2}. \tag{43}$$

An extreme combination $\tau = 10\,\mathrm{ms}$ and $\varepsilon_z = 1\,\mathrm{nm}$ raises the bound to $0.599\,\mathrm{MeV}$. These scales remain approximately 27 and 22 orders below the Planck energy, respectively. A Stern–Gerlach null result therefore constrains a low-energy or mesoscopic rotor gap; a Planck-scale gap would make the present correction negligible.

Modern coherent Stern–Gerlach interferometers demonstrate the field control needed for differential tests [4, 5, 6]. A practical analysis would use the measured mean of the two spin-resolved centroids, because the leading rotor force is common to both, and retain the branch separation as a simultaneous monitor of ordinary Pauli response.

6.5 Competing quadratic magnetic forces

The common potential is proportional to B^2, so conventional quadratic magnetic response must be included in the inference. Minimal coupling gives the atomic diamagnetic operator

$$H_{\mathrm{dia}} = \frac{e^2}{8m_e}\left[B^2 r^2 - (\boldsymbol{B}\cdot\boldsymbol{r})^2\right], \tag{44}$$

whose isotropic expectation is positive and therefore has the opposite sign to V_{c} [29]. Hyperfine mixing produces a further quadratic Zeeman coefficient whose magnitude and sign depend on the chosen state [30, 31]. Field-map error, gravity, velocity spread and detector response provide additional calibrated nuisance terms in matter-wave measurements [32].

These backgrounds suggest a discriminating protocol rather than a single species measurement. Atomic polarizabilities and quadratic Zeeman coefficients can be fixed by independent spectroscopy, while the candidate rotor contribution scales with the magnetic moment and a common Δ. A multi-species fit can therefore test whether a residual follows known atomic coefficients or the rotor-gap scaling of Eq. (24).

6.6 Scope

The present model is a nonrelativistic probe on a prescribed semiclassical background. Its centre parity, right weight, inertia and body-axis coupling define the effective sector; deriving them from the LQG Hamiltonian constraint is the next dynamical problem. Backreaction, graph refinement and relativistic production belong to that extension. Within the stated sector, the Pauli projection, finite-gap coefficients, coupling control and wave-packet remainder are fixed and independently reproducible.

7 Conclusions

A centre-odd, fixed-weight SU(2) rotor provides a two-dimensional $j = 1/2$ ground multiplet and a finite higher-spin tower. For a moment fixed to the rotor body axis, the standard direction-cosine projection fixes the Pauli interaction, while the $j = 3/2$ gap generates a common quadratic potential and a cubic spin correction. A generator-coupling control has the same Pauli block but no inter-multiplet response, identifying the body-axis operator as the source of the finite-gap physics.

Dressed two-dimensional propagation resolves both analytic terms. The total centroid follows Δ^{-1}, the cubic switch follows Δ^{-2}, and the full rotor agrees with the cubic effective Hamiltonian at an integrated density difference of 1.54×10^{-4} for the publication baseline. Separating bare higher-j weight from dressed leakage also shows that static dressing, rather than a transition, accounts for nearly all of the apparent excited-sector population.

Calibrating species-specific B^2 backgrounds turns the common-centroid shift into a direct gap bound. Its accessible scale is eV to sub-MeV for the laboratory examples considered here. The same construction supplies a concrete semiclassical target for framed SU(2) holonomy dynamics: derive, modify or exclude the body-axis finite-gap sector from an underlying node Hamiltonian.

A Representation and operator conventions

We use the spherical-vector convention

$$n_{\pm 1} = \mp \frac{n_x \pm i n_y}{\sqrt{2}}, \qquad n_0 = n_z, \tag{45}$$

so

$$n_x = \frac{n_{-1} - n_{+1}}{\sqrt{2}}, \qquad n_y = \frac{i(n_{-1} + n_{+1})}{\sqrt{2}}. \tag{46}$$

The exact matrix element is Eq. (8), with $q = 1/2$. We order the ground basis as

$$\left\{|\tfrac{1}{2}, \tfrac{1}{2}, q\rangle, |\tfrac{1}{2}, -\tfrac{1}{2}, q\rangle\right\}. \tag{47}$$

In this basis,

$$Pn_xP = \frac{1}{3}\begin{pmatrix} 0 & 1 \\ 1 & 0 \end{pmatrix}, \quad Pn_yP = \frac{1}{3}\begin{pmatrix} 0 & -i \\ i & 0 \end{pmatrix}, \quad Pn_zP = \frac{1}{3}\begin{pmatrix} 1 & 0 \\ 0 & -1 \end{pmatrix}. \tag{48}$$

The nonzero axial elements required through cubic order are

$$\langle \tfrac{3}{2}, \tfrac{1}{2}, q|n_0|\tfrac{1}{2}, \tfrac{1}{2}, q\rangle = \frac{\sqrt{2}}{3}, \tag{49}$$

$$\langle \tfrac{3}{2}, \tfrac{1}{2}, q|n_0|\tfrac{3}{2}, \tfrac{1}{2}, q\rangle = \frac{1}{15}, \tag{50}$$

with the corresponding diagonal signs reversed for $m = -1/2$. The numerical implementation verifies $n_p^\dagger = (-1)^p n_{-p}$ and $[J_i, n_j] = i\epsilon_{ijk}n_k$ exactly in symbolic arithmetic. Because the cutoff retains complete SU(2) multiplets, the vector commutator remains exact at finite $j_{\max}$; only identities requiring omitted neighbouring multiplets acquire cutoff residuals.

B Numerical convergence records

Table 2 gives observable-specific finest-pair changes. The domain sequence keeps the spatial spacing fixed. Values beneath the 10^{-8} absolute reporting floor remain in the table but are not used to assign significant digits.

The gap scan in Table 3 changes only Δ. The dressed spin-resolved columns use Eq. (26); the bare higher-j weight is listed as a dressing diagnostic.

Table 2: Relative finest-pair changes and the largest absolute change on each refinement axis.

Axis	$\delta\langle z\rangle$	Cubic switch	Bare high-j	Max. absolute
Spatial grid	1.42×10^{-14}	2.50×10^{-12}	4.84×10^{-14}	3.42×10^{-14}
Time step	3.55×10^{-8}	2.17×10^{-5}	3.25×10^{-5}	8.31×10^{-8}
Domain	1.19×10^{-8}	5.65×10^{-7}	2.33×10^{-10}	6.27×10^{-9}
Internal cutoff	4.23×10^{-7}	0	7.29×10^{-7}	1.27×10^{-7}

Table 3: Finite-gap scan with $r = \mu B_{\max}/\Delta$.

r	$\delta\langle z\rangle$	$\delta z_\uparrow$	$\delta z_\downarrow$	Cubic switch	$P^{\text{bare}}_{j\geq 3/2}$
0.01	-0.035920	-0.037149	-0.034738	1.295×10^{-5}	3.492×10^{-5}
0.02	-0.071847	-0.073955	-0.069833	5.188×10^{-5}	1.388×10^{-4}
0.04	-0.143684	-0.146495	-0.141066	2.081×10^{-4}	5.563×10^{-4}
0.06	-0.215430	-0.217530	-0.213626	4.693×10^{-4}	1.256×10^{-3}
0.08	-0.287010	-0.286985	-0.287434	8.356×10^{-4}	2.237×10^{-3}
0.10	-0.358334	-0.354787	-0.362389	1.307×10^{-3}	3.513×10^{-3}

Declarations

Funding. This research received no external funding.

Conflict of interest. The author declares no conflict of interest.

Data availability. The source code, numerical input parameters, machine-readable scan records, and source data for every figure are included in the accompanying reproducibility archive.

Author contribution. The author developed the model, performed the calculations, analysed the results, and wrote the manuscript.

References

[1] W. Gerlach and O. Stern. *Zeitschrift fur Physik* **9** 349 (1922).

[2] B. C. Hsu, M. Berrondo, and J.-F. S. V. Huele. *Physical Review A* **83** 012109 (2011).

[3] S. Krekels, C. Maes, K. Meerts, and W. Struyve. *Proceedings of the Royal Society A* **480** 20230861 (2024).

[4] S. Machluf, Y. Japha, and R. Folman. *Nature Communications* **4** 2424 (2013).

[5] O. Amit, Y. Margalit, O. Dobkowski, Z. Zhou, Y. Japha, M. Zimmermann, M. A. Efremov, F. A. Narducci, E. M. Rasel, W. P. Schleich, and R. Folman. *Physical Review Letters* **123** 083601 (2019).

[6] Y. Margalit, O. Dobkowski, Z. Zhou, O. Amit, Y. Japha, S. Moukouri, D. Rohrlich, A. Mazumdar, S. Bose, C. Henkel, and R. Folman. *Science Advances* **7** eabg2879 (2021).

[7] D. Bohm, R. Schiller, and J. Tiomno. *Nuovo Cimento Supplemento* **1** 48 (1955).

[8] D. Bohm, R. Schiller, and J. Tiomno. *Nuovo Cimento Supplemento* **1** 67 (1955).

[9] P. R. Holland. *Physics Reports* **169** 293 (1988).

[10] P. R. Holland. *The Quantum Theory of Motion*. Cambridge University Press, Cambridge, 1993.

[11] A. Ramsak. *Journal of Physics A: Mathematical and Theoretical* **45** 115310 (2012).

[12] C. H. Townes and A. L. Schawlow. *Microwave Spectroscopy*. McGraw-Hill, New York, 1955.

[13] J. M. Brown and A. Carrington. *Rotational Spectroscopy of Diatomic Molecules*. Cambridge University Press, Cambridge, 2003.

[14] S. A. Werner, R. Colella, A. W. Overhauser, and C. F. Eagen. *Physical Review Letters* **35** 1053 (1975).

[15] H. Rauch, A. Zeilinger, G. Badurek, A. Wilfing, W. Bauspiess, and U. Bonse. *Physics Letters A* **54** 425 (1975).

[16] C. Rovelli and L. Smolin. *Physical Review D* **52** 5743 (1995).

[17] A. Ashtekar and J. Lewandowski. *Classical and Quantum Gravity* **21** R53 (2004).

[18] T. Thiemann. *Classical and Quantum Gravity* **15** 1281 (1998).

[19] J. C. Baez and K. V. Krasnov. *Journal of Mathematical Physics* **39** 1251 (1998).

[20] M. Bojowald and R. Das. *Physical Review D* **78** 064009 (2008).

[21] C. Zhang, H. Liu, and M. Han. *Classical and Quantum Gravity* **40** 205022 (2023).

[22] J. R. Schrieffer and P. A. Wolff. *Physical Review* **149** 491 (1966).

[23] S. Bravyi, D. P. DiVincenzo, and D. Loss. *Annals of Physics* **326** 2793 (2011).

[24] E. R. Livine and J. Tambornino. *Journal of Mathematical Physics* **53** 012503 (2012).

[25] T. T. Wu and C. N. Yang. *Nuclear Physics B* **107** 365 (1976).

[26] D. A. Varshalovich, A. N. Moskalev, and V. K. Khersonskii. *Quantum Theory of Angular Momentum*. World Scientific, Singapore, 1988.

[27] M. D. Feit, J. A. Fleck, Jr., and A. Steiger. *Journal of Computational Physics* **47** 412 (1982).

[28] P. J. Mohr, D. B. Newell, B. N. Taylor, and E. Tiesinga. *Reviews of Modern Physics* **97** 025002 (2025).

[29] D. Delande and J. C. Gay. *Journal of Physics B: Atomic and Molecular Physics* **17** L335 (1984).

[30] G. Breit and I. I. Rabi. *Physical Review* **38** 2082 (1931).

[31] R.-B. Li, L. Zhou, J. Wang, and M.-S. Zhan. *Optics Communications* **282** 1340 (2009).

[32] A. D. Cronin, J. Schmiedmayer, and D. E. Pritchard. *Reviews of Modern Physics* **81** 1051 (2009).